PAPER • OPEN ACCESS

Linearised dynamics and non-modal instability analysis of an impinging under-expanded supersonic jet

View the article online for updates and enhancements.

IOP ebooks™

Bringing you innovative digital publishing with leading voices to create your essential collection of books in STEM research.

Start exploring the collection - download the first chapter of every title for free.

Linearised dynamics and non-modal instability analysis of an impinging under-expanded supersonic jet

Shahram Karami[1]**, Paul C. Stegeman**[1]**, Vassilis Theofilis**[2]**, Peter J. Schmid**[3] **, Julio Soria**[1,4]

[1]Department of Mechanical and Aerospace Engineering, Monash University, Melbourne, Australia
[2]School of Engineering, University of Liverpool, UK
[3]Department of Mathematics, Imperial College London, London, UK
[4]Department of Aeronautical Engineering, King Abdulaziz University, Jeddah, Kingdom of Saudi Arabia

E-mail: `shahram.karami@monash.edu`

Abstract. Non-modal instability analysis of the shear layer near the nozzle of a supersonic under-expanded impinging jet is studied. The shear layer instability is considered to be one of the main components of the feedback loop in supersonic jets. The feedback loop is observed in instantaneous visualisations of the density field where it is noted that acoustic waves scattered by the nozzle lip internalise as shear layer instabilities.

A modal analysis describes the asymptotic limit of the instability disturbances and fails to capture short-time responses. Therefore, a non-modal analysis which allows the quantitative description of the short-time amplification or decay of a disturbance is performed by means of a local far-field pressure pulse. An impulse response analysis is performed which allows a wide range of frequencies to be excited. The temporal and spatial growths of the disturbances in the shear layer near the nozzle are studied by decomposing the response using dynamic mode decomposition and Hilbert transform analysis.

The short-time response shows that disturbances with non-dimensionalised temporal frequencies in the range of 1 to 4 have positive growth rates in the shear layer. The Hilbert transform analysis shows that high non-dimensionalised temporal frequencies (>4) are dampened immediately, whereas low non-dimensionalised temporal frequencies (<1) are neutral. Both dynamic mode decomposition and Hilbert transform analysis show that spatial frequencies between 1 and 3 have positive spatial growth rates. Finally, the envelope of the streamwise velocity disturbances reveals the presence of a convective instability.

1. Introduction

The scenario of a supersonic jet impingement on a ground surface is inevitable in new aircraft technologies where short distance and vertical take-offs and landings are desirable. The intense pressure waves in such flows result in numerous challenges. The high level of oscillations on the landing surface damages the surface structure and can lead to fatigue of the aircraft structure as the pressure waves are reflected by the surrounding surfaces. Environmental and safety problems need to be addressed because the resulting noise and pressure waves are intense. The impingement creates an extremely complicated flow field with a number of interconnected flow
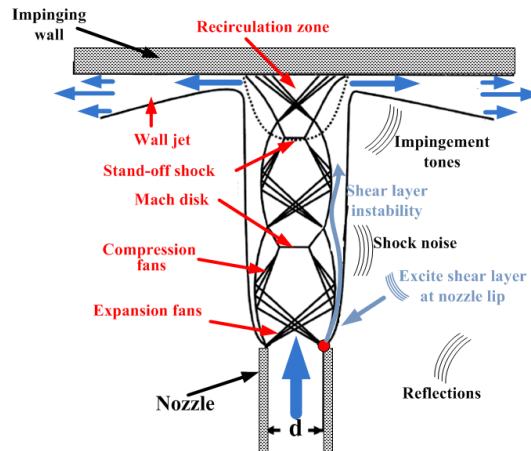
Figure 1: Schematic of a impinging jet.

physics involved. Specifically, development of shear layer instabilities that evolve into vortices, vortex-shock interaction, as well as an axisymmetric stagnation flow and a wall jet are present in this flow.

An important phenomenon is the instability waves that are the result of acoustic waves being scattered by the nozzle lip and grow as they propagate in the shear layer of the jet which is sketched in figure 1. The interactions of the sound and the jet form a feedback loop. The shear-layer disturbances develop in the form of a Kelvin-Helmholtz instability and interact with the Mach disk and stand-off shock which produces shock movements that alter the flow characteristics. This pulsatile motion creates high intensity acoustic waves which travel upstream and perturb the shear layer, closing the feedback loop. Considerable evidence for the feedback loop being the mechanism responsible for the self-sustained oscillations has been accumulated in a number of experimental studies of supersonic impinging jets [1, 2, 3, 4, 5, 6]. However, our understanding of the feedback loop is not complete as the process is sensitive to jet inlet conditions and geometrical boundary conditions. The flow field and hence, the level of pressure oscillations depend on the nozzle pressure ratio (NPR)[1] and the distance between the nozzle exit and the wall. The instability is intensified when the nozzle exit to wall distance (h/d) is shorter than the potential core [2] [7, 8]. In experimental studies of under-expanded supersonic impinging jets with NPR $\approx$ 4, three tone-producing regimes are observed. Symmetrical oscillations occur for $x/d < 2.7$, a zone of silence takes place for $2.7 < x/d < 3.5$, and normal tone-producing regimes are active for $3.5 < x/d < 3.8$ [7].

The propagation of the instabilities that were internalised due to the acoustic waves being scattered by the nozzle lip is one of the main components of the feedback loop. The time development of these instabilities can be modeled by linearised Navier Stokes equations. Depending on the research questions two main approaches have been developed to study the process. The first class of the linear stability analysis which deals with the response behaviour of the base flow to disturbances as time approaches to infinity is called modal analysis [9]. The second method is interested in the short-time behaviour of disturbances known as non-modal analysis. Comprehensive reviews of the modal and non-modal methods are presented in the review papers by Theofilis [10] and Schmid [11], respectively. The modal instability analysis

---

[1] The nozzle pressure ratio (NPR) is here defined as the ratio between the stagnation pressure measured in the jet plenum and the ambient pressure.
[2] The potential core of the jet is the distance from the nozzle where the jet centerline velocity is relatively constant.

leads to a generalized large-scale eigenvalue problem. A solution of this sparse eigenvalue problem provides the modal frequencies and amplification/damping rates. Therefore, the modal instability analysis describes the asymptotic fate of the perturbation. It appears that this asymptotic solution and the shape of the least stable mode may not describe the overall perturbation dynamics accurately and analysis of the instability growth and decay in a finite-time horizon is necessary [11]. Therefore, the subsequent non-modal shear layer instability, which explains the short-time responses of the shear layer to external disturbances, is the principle gap that the present paper tries to address.

2. Governing equations

The compressible conservation equations of mass, momentum, and total energy in cylindrical coordinates are the governing equations that apply to supersonic under-expanded impinging jets. These equations are non-dimensionalised with respect to the ambient conditions. The non-dimensional variables are defined as follows,

$$\mathbf{x} = \frac{\mathbf{x}_j^*}{d}, \quad \mathbf{u} = \frac{\mathbf{u}^*}{a_o^*}, \quad \rho = \frac{\rho^*}{\rho_o^*}, \quad t = \frac{t^* a_o^*}{d}, \quad p = \frac{p^*}{\rho_o^* a_o^{*2}},$$

$$T = \frac{T^*}{T_o^*}, \quad \mu = \frac{\mu^*}{\mathrm{Re}\mu_o^*}, \quad \mathrm{Pr} = \frac{v^*}{\alpha^*}, \quad M_o = \frac{a_o^*}{\sqrt{RT_o^*}} \quad \mathrm{Re} = \frac{\rho_o^* a_o^* d}{\mu_o^*}. \tag{1}$$

Here, the superscripts '*' and 'o' represent the dimensional values and ambient conditions, respectively. $\mathbf{x}$ represents the spatial vector; $\mathbf{u}$ the velocity vector; d the jet diameter (see figure 3); a the speed of sound; ρ the density; T the temperature; t the time; p the pressure; and μ the dynamic viscosity, which is given by $\mu/\mu_o = (T/T_o)^{0.7}$ [12]. The variable Re represents the Reynolds number and Pr the Prandtl number. The non-dimensional forms of the equations are

$$\frac{\partial \rho}{\partial t} = -\nabla \cdot (\rho \mathbf{u}), \tag{2}$$

$$\frac{\partial \rho \mathbf{u}}{\partial t} = -\nabla \cdot (\rho \mathbf{u} \otimes \mathbf{u} + p\mathbb{I} - \mu\mathbb{T}),$$

$$\frac{\partial \rho e}{\partial t} = -\nabla \cdot \left[\mathbf{u}(\rho e + p) - \mathbf{q} - \mu\mathbb{T} \cdot \mathbf{u} \right].$$

where the deviatoric stress tensor, $\mathbb{T}$, and heat flux, $\mathbf{Q}$ are defined as

$$\mathbb{T} = \left[\nabla\mathbf{u} + (\nabla\mathbf{u})^T + \left(\frac{\mu_b}{\mu} - \frac{2}{3} \right)(\nabla \cdot \mathbf{u})\mathbb{I} \right], \tag{3}$$

$$\mathbf{Q} = \frac{\mu\gamma}{\gamma - 1} \frac{1}{M_o^2 Pr} \nabla T.$$

Here, $\gamma = 1.4$ is the heat capacity ratio of air, e is the sensible energy, and the density weighted sensible energy is given by

$$\rho e = \frac{1}{2}\rho\mathbf{u} \cdot \mathbf{u} + \frac{\rho T}{M_o^2(\gamma - 1)} = \frac{1}{2}\rho\mathbf{u} \cdot \mathbf{u} + \frac{p}{\gamma - 1}. \tag{4}$$

The ideal gas assumption is used in this study and the equation of state is $p = \rho T/M_o^2$. Further details of the equations in cylindrical coordinates are found in Ref. [13]. Equation (2) is commonly presented as an evolution equation in the following compact form

$$\frac{\partial \mathbf{Q}}{\partial t} = \mathbf{F}(\mathbf{q}), \tag{5}$$

From which the linearised Navier Stokes equations (LNSE) are derived by superimposing small amplitude disturbances on a mean flow. Denoting the mean flow variables as $\overline{(...)}$ and perturbations as $(...)'$, the linearised Navier Stokes equations are given as

$$
\begin{aligned}
\frac{\partial \rho'}{\partial t} &= -\nabla \cdot (\rho \mathbf{u})', \\
\frac{\partial (\rho \mathbf{u})'}{\partial t} &= -\nabla \cdot \left(\overline{\rho \mathbf{u}} \otimes \mathbf{u}' + (\rho \mathbf{u})' \otimes \overline{\mathbf{u}} \right) - \nabla p' + \overline{\mu} \nabla \cdot \mathbb{T}', \\
\frac{\partial (\rho e)'}{\partial t} &= -\nabla \cdot \left(\overline{(\rho e + p)} \mathbf{u}' + (\rho e + p)' \overline{\mathbf{u}} \right) + \overline{k} \nabla^2 T' + \overline{\mu} V_{KE},
\end{aligned}
\tag{6}
$$

where

$$
\begin{aligned}
V_{KE} &= \left((\nabla \cdot \mathbb{T}') \cdot \overline{\mathbf{u}} + (\nabla \cdot \mathbb{T}') \cdot \mathbf{u}' + \mathbb{T}' : \nabla \overline{\mathbf{u}} + \overline{\mathbb{T}} : \nabla \mathbf{u}' \right), \\
\mathbb{T} &= \nabla \mathbf{u} + (\nabla \mathbf{u})^T + \left(\frac{\mu_B}{\mu} - \frac{2}{3} \right) (\nabla \cdot \mathbf{u}) \, \mathbb{I}, \\
(\rho e)' &= \frac{1}{2} \rho \|\mathbf{u}'\|^2 + \frac{p'}{\gamma - 1},
\end{aligned}
\tag{7}
$$

and the linearised version of the equation of state is

$$
p' = \frac{\overline{\rho} T' + \rho' \overline{T}}{M_0^2}.
\tag{8}
$$

Finally, the viscosity and thermal conductivity are given by

$$
\overline{\mu} = \frac{\overline{T}^{0.76}}{Re} \qquad \text{and} \qquad \overline{k} = \overline{\mu} \frac{\gamma}{\gamma - 1} \frac{1}{M_0^2 Pr}.
\tag{9}
$$

These equations are the LNSE, commonly presented in the concise matrix form

$$
\frac{\partial q'}{\partial t} = \mathbb{A} q',
\tag{10}
$$

where q' is the perturbations $(\rho', u'_x, u'_r, u'_\theta, e')$, and $\mathbb{A}$ is the linear operator advancing the small perturbation in time.
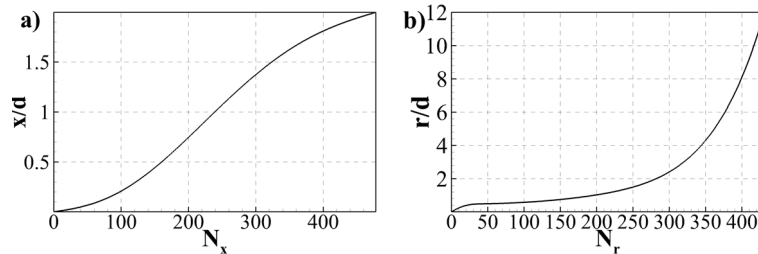

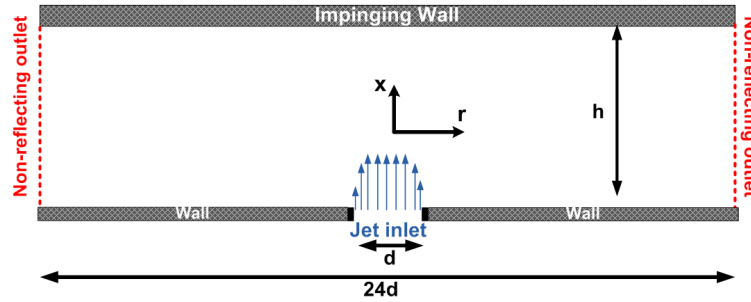Figure 2: Location of the computational grid points in (a) axial and (b) radial directions.

Figure 3: Schematic of the domain and the configuration of this study.

2.1. Configuration and numerical methods

The configuration is an under-expanded impinging jet with a close nozzle–to–wall distance of $h/d=2$ and a radial domain of 12d (figure 3). To obtain the mean flow field (q), an in-house developed high-fidelity LES parallel code that has been tested and validated in previous studies [14, 15, 16, 17] is used to solve the filtered partial differential equations presented in equation (2) with the subgrid scale terms being computed using Germano's dynamic model with the adjustment proposed by Lilly [18]. A sixth-order central finite difference method is applied in the smooth regions in the spatial directions while a fifth-order weighted essentially non-oscillating scheme with local Lax-Friedrichs flux splitting is used in the discontinuous regions. The temporal integration is performed using a fourth-order five-step Runge-Kutta scheme [19, 20]. There are $N_x \times N_r \times N_\theta = 480 \times 400 \times 96$, computational grid points in the LES. A uniform grid is employed in the azimuthal direction. In the axial direction, stretch grid points are used with two stretching rates. A fine grid is used near the nozzle and the impinging wall. A fine grid point of approximately $0.001d$ is employed in the mixing layer with a polynomial stretch of the grids towards the centre of the jet and far-field. The locations of the radial and axial grids are shown in the figure 2 for the sake of completeness. The locally one-dimensional inviscid compressible boundary condition proposed by Poinsot [21] is employed at the outflow boundaries. In addition, the optimised sponge region of Mani [22] is employed near the outflow boundaries to minimise the reflections from the outflow boundaries. In the sponge regions, the flow field is forced to a self-similar solution which was determined a priori. The mean inlet axial velocity U_{in} is specified using the hyperbolic-tangent function of Ref. [23] given by

$$\frac{U_{in}}{U_j} = \frac{1}{2} \left(1 - \tanh \left[\frac{1}{4\delta_{in}} (\frac{r}{r_j} - \frac{r_j}{r}) \right] \right), \tag{11}$$

where U_j is the jet inlet velocity, r_j the jet inlet radius and δ_{in} the inlet momentum (mixing layer) thickness. The inlet momentum thickness is equal to $0.04d_j$ in this simulation. The inlet velocity is free of any synthetic turbulence. The Reynolds number is 50,000, the Mach number is 1.0, and the ratio between the stagnation pressure measured in the jet plenum and the ambient pressure (NPR) is 3.4.

The linearised Navier Stokes equations (equation 6) are solved with the same LES resolution in a smaller domain in the radial direction. A sixth-order central finite difference method and fourth-order five-step Runge-Kutta are used for the spatial discretisation and temporal integration, respectively [14]. The mean field obtained from the LES by an ensemble averaging of the data over 38 jet times with the jet time is defined as h/U_j, where h is the impingement wall distance from the nozzle and U_j is the jet bulk velocity in the inlet.

2.1.1. Dynamic Mode Decomposition (DMD)

Dynamic mode decomposition (DMD) is a powerful diagnostic technique which can reveal the spatial and temporal dynamics of coherent structures in fluid flows. The technique relies on sequential snapshots of the flow without any information about the underlying governing equations. Therefore, it can be used in both experimental and numerical studies. Since proposed by Schmid [24], it has been used to study a wide range of fluid flow problems [24, 25, 26, 27]. The concept is similar to the Arnoldi algorithm where a low-dimensional approximation of the high-dimension linear operator is obtained through orthogonalisation techniques. The flow field variables with underlying phenomena of interest are collected by sampling either from a numerical simulation or an experimental measurement in a form of sequential snapshots. These snapshots form a matrix

$$\Psi = \psi_1, \psi_2, ..., \psi_n, \tag{12}$$

where the snapshots, ψ_i have a same time interval Δt. The snapshots are assumed to be linearly related

$$\psi_{i+1} = A\psi_i, \tag{13}$$

Splitting Ψ into two subspaces of $\Psi_1 = \psi_1, \psi_2, ..., \psi_{n-1}$ and $\Psi_2 = \psi_2, \psi_3, ..., \psi_n$, the linear mapping implies that

$$\Psi_2 = \mathbf{A}\Psi_1 + \mathbf{r}, \tag{14}$$

where $\mathbf{r}$ is the residual and represents the deviation of the system from the linear assumption. In this study, DMD applies to the time series obtained from the solution of the linearised Navier Stokes equations; therefore, the residual is considered to be zero. The SVD-based approach is used in this study [24]. The aim is the construction of a low-dimension matrix S through the similarity transform of A. The procedure is as follows. Assume that the SVD of Ψ_1 is given as $U\Sigma W^T$. Then,

$$\Psi_2 = \mathbf{A}\Psi_1 = \mathbf{A}U\Sigma W^T, \tag{15}$$

Pre-multiplying both sides of equation (15) by U^T and post-multiply by $W\Sigma^{-1}$ noting that the columns of U are the left singular vectors and the rows of W^T are the right singular vectors, yields

$$U^T A U = U^T \Psi_2 W\Sigma^{-1} \equiv S. \tag{16}$$

Matrix S has the same eigenvalues as A because it is obtained through similarity transformation and the eigenvectors are related by a factor of U. The DMD approach is used in this study to obtain both temporal and spatial growth rates in the shear layer. It should be noted that the disturbances are considered to have a temporal form given by

$$q' = \hat{q}(x, r)e^{(\omega_r + i\omega_i)t}e^{im\theta}, \tag{17}$$

for the temporal instability analysis, while they have a spatial form given by

$$q' = \hat{q}(r, t)e^{(\alpha_r + i\alpha_i)x}e^{im\theta}, \tag{18}$$

for the spatial instability analysis. Here, ω_i is the temporal frequency, ω_r the temporal growth rate, α_i the spatial frequency and α_r the spatial growth rate. The azimuthal mode number, m, is considered to be zero in the present study.

2.1.2. Hilbert transform analysis

The Hilbert transform is used to create an analytic signal. For signal $u(t)$, given its Hilbert transform $\hat{u}(t)$, the analytical signal is defined as the composition,
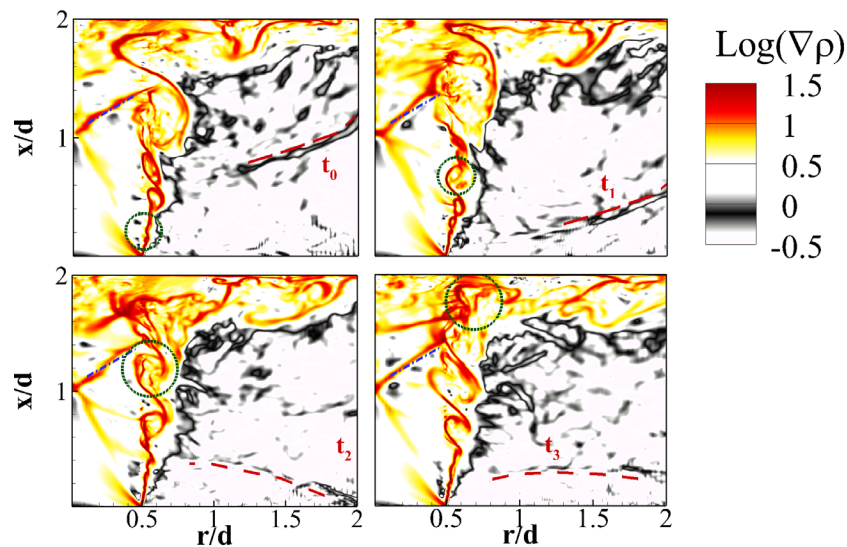
$$u_a(t) = u(t) + i\hat{u}(t), \tag{19}$$

Figure 4: Instantaneous contour plots of logarithm of the density gradient magnitude (Colorbar adjusted to separate the strong gradient regions (hydrodynamic driven gradient) from low gradient regions (acoustic driven gradients), the dash-dot blue lines have fixed locations, the propagating acoustic waves are highlighted by dashed red poly-lines.

which can be expressed in exponential notation as $u_a(t) = K(t)e^{i\phi(t)}$, where $K(t)$ is the instantaneous amplitude or envelop of the signal and $\phi(t)$ is the instantaneous phase. The instantaneous frequency of the signal is also available given by,

$$f(t) = \frac{1}{2\pi}\frac{d\phi}{dt}. \tag{20}$$

The Hilbert transform analysis in this study is applied to answer two questions. First, what are the trailing edge, leading edge and group velocities of the wave packets? Second, how does the energy of the waves with different frequencies evolve temporally and spatially?

3. Results and Discussion
3.1. Large eddy simulation
The instantaneous flow fields are presented in this section to illustrate the complexity present in the under-expanded supersonic impinging jet. Figure 4 shows the contour plots of instantaneous density gradient for the sequences of t_0 to t_3. The contour level is in a log scale with two color scales to facilitate the visualisation of the processes. The regions with high gradients are in red/yellow color while the low gradient regions are in black/grey color. The high gradients represent the Kelvin-Helmholtz structures as well as the shock cells. As can be seen, an inviscid instability of the Kelvin–Helmholtz type is initiated as marked by a green circle in the first instant and a vortex is created and convected as growing in the shear layer (next two time sequences) which is similar to previous observations in the experimental and numerical studies of free and impinging jets [28, 29, 30, 3] and jets in crossflow [31, 32]. This process is followed by an interaction of the vortex with the stand-off shock which has been observed in experimental and numerical studies of impinging jets [28, 29, 30, 3]. The low gradient regions are associated with propagations of acoustic waves. The acoustic waves of impingement propagates towards the inlet as in the first two instants in figure 4 and then reflects from the boundaries (last two instants in figure 4). The self-sustained process of a Kelvin–Helmholtz instability development in the shear layer of the jet followed by acoustic wave generation and propagation towards the
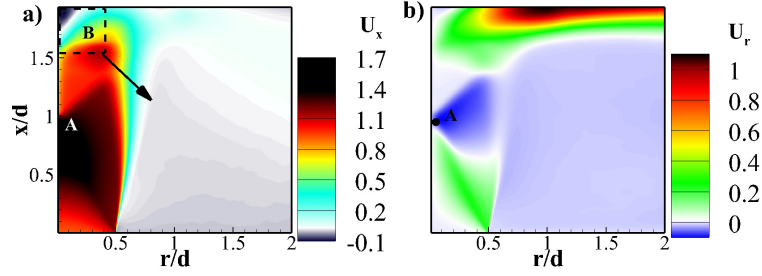
Figure 5: The ensemble averages of (a) streamwise and (b) radial velocity fields (with a zoom of the velocity streamlines in the recirculation region.).
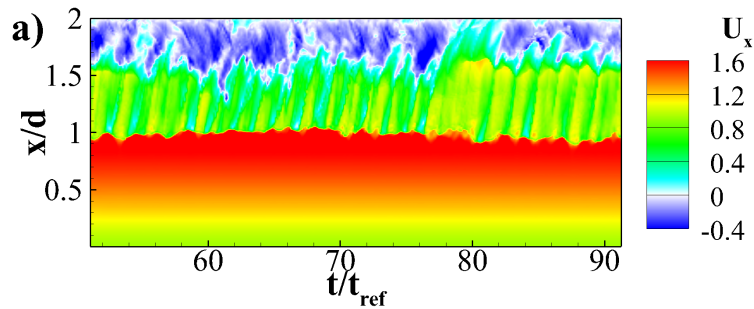

Figure 6: The history of the centreline streamwise velocity.

nozzle has been a topic of research for a few decades and is commonly explained by the feedback loop mechanism [33, 30, 2, 3]. However, the process of completing the feedback loop is still a subject of debate. It is commonly accepted that excitation of the shear layer instability by acoustic waves is one of the main component of the loop. Therefore, the focus of the next sections is on the short-time response of the shear layer to external acoustic waves through the solution of the linearised Navier Stokes equations with an initial acoustic pulse. A base flow is required for this purpose which we will consider to be the temporal average of the LES results.

3.1.1. Mean flows

Figure 5 presents the ensemble averages of streamwise and radial velocity fields. The ensemble averages are computed as simultaneous temporal and azimuthal direction means. For the sake of completeness the time history of the centreline streamwise velocity is presented in figure 6 which clearly shows the solution is reached the steady state condition. A sudden drop in streamwise velocity at $x/d \approx 1$ is observed in figure 5, marked as 'A' and indicates the Mach disk. The streamwise velocity also shows a local increase near to the wall, which is associated with the bow or stand-off shock. A recirculation region exists between the bow shock and the impinging wall. The streamlines in this region marked as 'B' is also shown in figure 5a where the circulation is clearly observable. Figure 5b shows the mean radial velocity. The formation of a wall jet flow is also observed as the radial velocity is positive in the region away from the stagnation point.

3.2. Linearised impulse response of the base flow

The response of the mean flow field to an axisymmetric acoustic pressure pulse in the form of an initial value problem is performed in this section. The linearised Navier-Stokes equations given by equation 6 are solved with an initial pressure pulse described by,

$$p'_{@(t=0)} = A \, exp\left(-\frac{(x-x_o)^2}{2\sigma_x^2} - \frac{(r-r_o)^2}{2\sigma_r^2}\right), \tag{21}$$
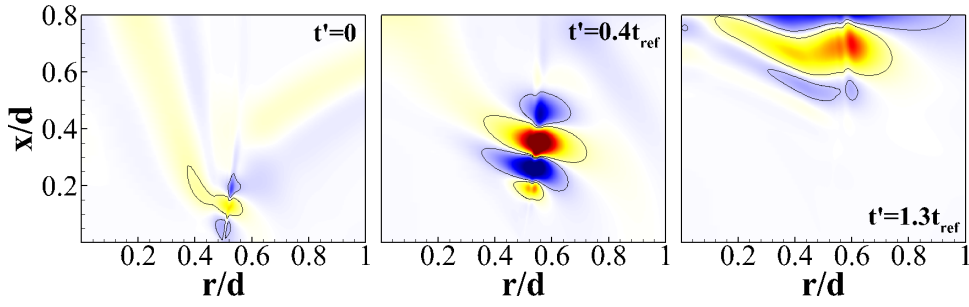
Figure 7: Instantaneous streamwise component of the velocity disturbance.

where 'A' is the amplitude of the pulse; x_o and r_o are the streamwise and radial location of the centre of the pulse, respectively; σ_x and σ_r are the radii of the pulse in the streamwise and radial directions, respectively. The pulse excites a broad range of frequencies and both the temporal and spatial growth rates as a function of frequency can be recovered by DMD and the Hilbert transform analysis. The Hilbert transform analysis is valid in this context as the signals are generated by a linear mapping and have mean values of zero.

The mean velocity field (figure 5) shows that the Mach disk is located at x/d≈1.0. Therefore, the region and time of the DMD and Hilbert transform analysis should be bounded to avoid nonlinearity effects of the Mach disk on the results. To facilitate this, data for spatio-temporal linear stability is collected in the region from the nozzle lip to 0.8d downstream of the nozzle lip just before the Mach disk location. The time is also limited to the time frame between the time disturbance hits the nozzle lip and the time at which it passes x=0.8d. The time evolution of the disturbance is presented in figure 7, where t' is zero when the disturbance forms at the nozzle lip. The time period used in this analysis is more comprehensible in the time history of the velocity disturbance on the shear layer of the jet, as shown in figure 8. The data used for the DMD and Hilbert transform analysis are considered in the time frame between t_0 and t_n in figure 8.
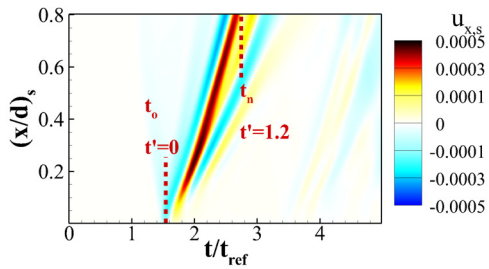

Figure 8: Time history of the streamwsie velocity disturbances on the shear layer of the jet.
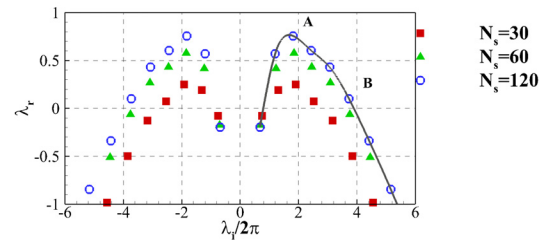

Figure 9: Temporal growth rate obtained from dynamic mode decomposition of linearised responses to pressure pulse.

3.2.1. Dynamic mode decomposition

Dynamic mode decomposition is used for both temporal and spatial linear stability analysis. Temporal decomposition is discussed first, where sequences of streamwise velocity fluctuation snapshots are used as the base for the dynamic mode decomposition. It is expected that by increasing the number of flow fields in our sequence, eigenvalues of the reduced order matrix S converge towards eigenvalues of the linear operator [24]. The convergence behaviour of the dynamic mode decomposition as the number of snapshots increases (i.e. interval of the snapshots decreases) is presented in Figure 9, where the temporal growth rates are shown as a function

of temporal frequencies. It is clear that an increase in the number of snapshots improves the convergences and that 120 snapshots are sufficient for the purpose of this study. Before we discuss the findings, a caveat is that this analysis has been performed for the short period of time between the formation of the shear layer instability and appearance of the developed disturbance at the Mach disk location. Therefore, the findings are limited to this short period and should not be compared to the *global modes*. Figure 9 shows that disturbances within the non-dimensionalised frequency band of 1–4 grow exponentially, while other frequencies are damped. This result highlights the natural responses of the shear layer of this under-expanded supersonic jet during the evolution of disturbances in the shear layer. The most remarkable finding is that only the disturbance within the non-dimensionalised frequency band of 1–4 grow in this short period. Figures 10 and 11 show the real part of the dynamic modes 'A' and 'B' in Figure 9. The amplitude of the low frequency mode 'A' is stronger and more developed throughout the shear layer, whereas the amplitude of the high frequency mode 'B' is much weaker and waves initially grow in the shear layer and then half way through after reaching a maximum amplitude, they decay.
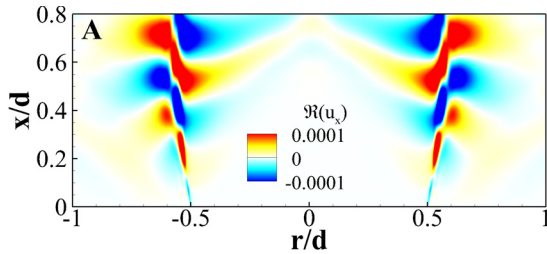

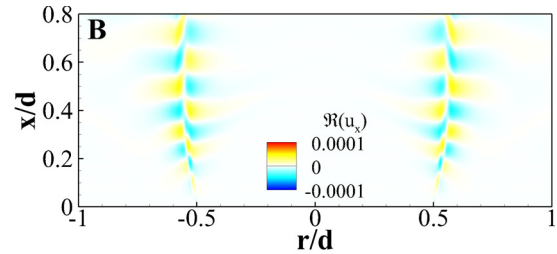Figure 10: The real part of the dynamic mode 'A' in figure 9.

Figure 11: The real part of the dynamic mode 'B' in figure 9.

The spatial growth rate obtained using DMD, where the snapshots are in radial-time coordinate and ordered incrementally in the streamwise direction, is shown in figure 12 as a function of spatial frequencies. The waves with low spatial frequencies (i.e. long wavelengths) have the highest growth rates. On the other hand, waves with high spatial frequencies (i.e. short wavelengths) have low growth rates. This behaviour is expected as the large structures have a high tendency to grow in the direction of the flow motion before the vortex breakdown process which is usually after the potential core. This agrees also with your findings in figure 4, where it is possible to see that the vortex is growing as it is convected.

The summary of the findings of the dynamic mode decomposition are as follows: the waves with streamwise wavelengths ($2\pi/\alpha_i$) of more than approximately 1/8 will grow in the streamwise direction if they have non-dimensionalised temporal frequency in the range of approximately 1 to 4. The overlap is for the non-dimensionalised temporal frequency approximately less than
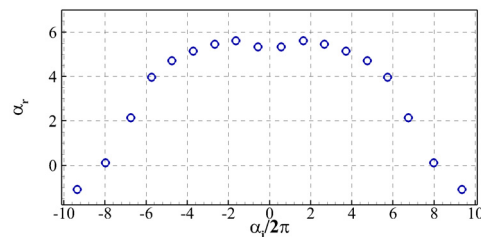

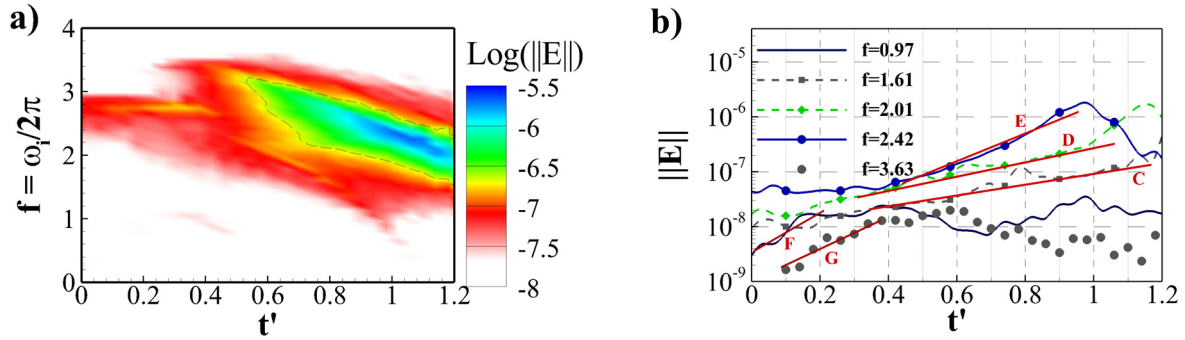Figure 12: Spatial growth rate obtained form DMD.

Figure 13: a) Energy as function of time and frequency and b) Time evolution of energy of different frequencies obtained from Hilbert transform analysis.

1. This conveys that the low spatial wavelengths may grow as they progress in the shear layer; however, they decay as time elapses.

3.2.2. Hilbert transform analysis

The dynamic mode decomposition analysis presented in the previous section provides interesting information about spatio-temporal growth rates. This section of the paper tries to further clarify the spatio-temporal non-modal instability by using the Hilbert transform analysis of streamwise velocity perturbation where both time and frequency appear as independent variables. The streamwise velocity perturbation is a function of time and space. To perform the analysis, Hilbert transform was applied to the time dependent signal at each grid point in the domain of interest. The analytical signal is obtained for each spacial location. This analytical signal is a function of time, frequency and space. The energy of the signal is defined as the square of the amplitude of the signal. Depending on whether the analysis performed for the spatial or the temporal instability, the energy is conditionally accumulated in time or space for each frequency.

The contour plot of energy of the perturbation conditionally accumulated on frequency and time is presented in Figure 13a. The waves with non-dimensional frequencies in the range of 1.5–3.2 contain 90% of the total energy. This confirms the dominant roles of these frequencies obtained by DMD (see Figure 9). Temporal evolutions of the conditionally accumulated energy for a few non-dimensional frequencies are presented in Figure 13b which shows that the non-dimensional frequencies denoted as 'C', 'D', and 'E' (in the range of 1.5–3.2) have positive growth rates. It is interesting to note that non-dimensional frequencies less than approximately 1 and higher than approximately 3.2 (marked by 'F' and 'G'), show positive growth in the beginning of the process ($t' < 0.4$) and thereafter they are either damped for the high frequencies or neutral for the low frequencies.

The contour plot of energy of the perturbation conditionally accumulated over spatial frequencies and streamwise locations is presented in Figure 14. This figure shows that high spatial frequencies (i.e. short wavelengths) are formed near the nozzle. These waves are damped as they propagate downstream. The disturbances with the wavelengths in the range of 1/3 to 1 contain most of the energy. The energy of these waves grows in streamwise direction. The spatial frequencies less than 0.5 (i.e. wavelengths longer than 1) do not contain any energy. The findings of the Hilbert transform analysis analysis are summarised as follows: the disturbances with streamwise wavelengths ($2\pi/\alpha_i$) between 1/3 and 1 grow in the streamwise direction and the disturbances with non-dimensionalised temporal frequencies in the range of approximately 1.5 to 3.2 grow by time.

It is informative to present the space-time properties of the envelope of the streamwise
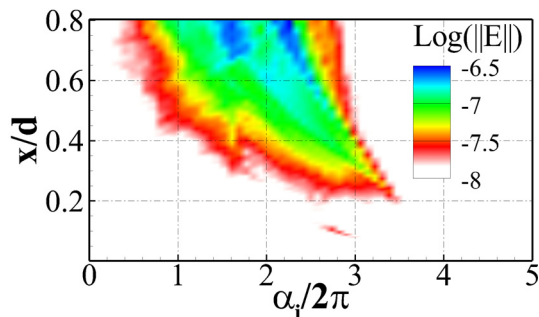
Figure 14: Energy as function of spatial frequency and streamwise location obtained from Hilbert transform analysis.
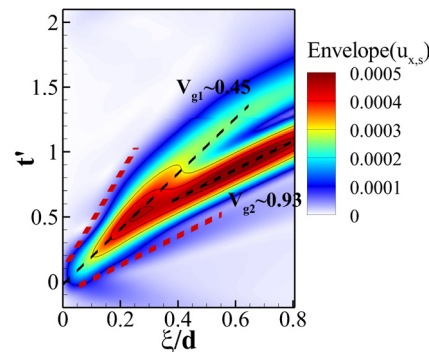

Figure 15: Envelop of the streamwise velocity along the shear layer trace.

velocity perturbation to get a better picture of the spatio-temporal growth. The envelope of the streamwise velocity perturbation along the shear layer of the jet [3] obtained from the Hilbert transform analysis is presented in Figure 15. The leading-edge and trailing-edge of the wave have positive velocities which indicate a convective instability in the shear layer which was also observed in our previous study [14] for a different nozzle–to–wall distance. It is notable that the group velocity, defined as the slope of the curve tracking the maximum value of the envelope, changes along the shear layer. The wave packet seems to split as it progresses in the shear layer, and the high amplitude trace is convected with velocity close to the speed of the sound while the low amplitude trace travels with velocity close to the mean convective velocity of the shear layer. This clearly shows the dispersive characteristic of the shear layer and also indicates that the wave packets are hydrodynamic waves in the region close to the nozzle lip while they split downstream into both acoustic and hydrodynamic waves.

4. Conclusions

The spatio-temporal characteristic of the shear layer of an under-expanded supersonic impinging jet has been studied.

A non-modal instability analysis is conducted for the shear layer near the nozzle. To avoid the non-linear effects of shocks, the analysis is limited to a domain between the nozzle lip and and 0.8d downstream of the nozzle lip, as well as the time period in which these disturbances evolve within the shear layer. Both DMD and Hilbert transform analysis show that the frequency band of the shear layer response is in the range of non-dimensional frequencies between approximately 1 and 4. This temporal analysis suggests that if the mean field is perturbed by selective frequencies with the same amplitudes, waves within this range of frequencies will grow exponentially in the shear layer near the nozzle and for the time period of their evolution in the shear layer before reaching the Mach disk location. The spatial DMD analysis reveals that the disturbances with non-dimensionalised wavelengths less than 1/8 will be dampened immediately while other spatial-waves grow in the streamwise direction. The results obtained from the Hilbert transform analysis show that the spatial frequencies between 1 and 3.5 (i.e. non-dimensionalised wavelengths between 0.28 and 1) contain most of the energy of the disturbances. Finally, the envelope of the streamwise velocity disturbances obtain from Hilbert transform at the shear layer confirms the presence of a convective instability.

---

[3] The axis ζ is tangential to the shear layer of the jet.

References

[1] Henderson B, Bridges J and Wernet M 2005 *J. Fluid Mech.* **542** 115–137
[2] Henderson B and Powell A 1993 *J. Sound Vib.* **168** 307–326
[3] Edgington-Mitchell D, Honnery D R and Soria J 2012 *J. Visual.-Japan* **15** 333–341
[4] Mason-Smith N, Edgington-Mitchell D, Buchmann N A, Honnery D R and Soria J 2015 *Shock Waves* **25** 611–622
[5] Weightman J, Amili O, Honnery D, Edgington-Mitchell D and Soria J 2015 *Australian Conf. Laser Diagnostics in Fluid Mech. and Combustion* (Monash Univ. Pub.) pp 167–172
[6] Weightman J, Amili O, Honnery D, Edgington-Mitchell D and Soria J 2017 *23rd AIAA/CEAS Aeroacoustics Conf.* p 3031
[7] Dauptain A, Cuenot B and M Gicquel L 2010 *AIAA J.* **48** 2325–2338
[8] Ho C M and Nosseir N S 1981 *J. Fluid Mech.* **105** 119–142
[9] Pierrehumbert R and Widnall S 1982 *J. Fluid Mech.* **114** 59–82
[10] Theofilis V 2011 *Annu. Rev. Fluid Mech.* **43** 319–352
[11] Schmid P J 2007 *Annu. Rev. Fluid Mech.* **39** 129–162
[12] Karami S, Hawkes E R, Talei M and Chen J H 2015 *J. Fluid Mech.* **777** 633–689
[13] Constantinescu G S and Lele S K 2002 *J. Comput. Phys.* **183** 165–186
[14] Stegeman P C, Pérez J M, Soria J and Theofilis V 2016 *J. Phys. Conf. Ser.* **708** 012015
[15] Stegeman P C, Soria J and Ooi A 2016 *Fluid-Structure-Sound Interactions and Control* (Springer) pp 241–245
[16] Stegeman P C, Ooi A and Soria J 2015 *Instability and Control of Massively Separated Flows* (Springer) pp 85–90
[17] Stegeman P C, Soria J and Ooi A 2014 *19th Australasian Fluid Mech. Conf.*
[18] Lilly D K 1992 *Phys. Fluids A* **4** 633–635
[19] Kennedy C A and Carpenter M H 1994 *Appl. Numer. Math.* **14** 397 – 433
[20] Kennedy C A, Carpenter M H and Lewis R M 2000 *Appl. Numer. Math.* **35** 177 – 219
[21] Poinsot T and Lele S K 1992 *J. Comput. Phys.* **101** 104 – 129
[22] Mani A 2012 *J. Comput. Phys.* **231** 704–716
[23] Bodony D J and Lele S K 2005 *Phys. Fluids* **17** 085103
[24] Schmid P J 2010 *J. Fluid Mech.* **656** 5–28
[25] Muld T W, Efraimsson G and Henningson D S 2012 *Comput. Fluids* **57** 87–97
[26] Duke D, Honnery D and Soria J 2012 *J. Fluid Mech.* **691** 594–604
[27] Grilli M, Schmid P J, Hickel S and Adams N A 2012 *J. Fluid Mech.* **700** 16–28
[28] Edgington-Mitchell D, Oberleithner K, Honnery D R and Soria J 2014 *J. Fluid Mech.* **748** 822–847
[29] Krothapalli A, Rajkuperan E, Alvi F and Lourenco L 1999 *4th AIAA/CEAS Aeroacoustics Conf.* p 2239
[30] Elavarasan R, Krothapalli A, Venkatakrishnan L and Lourenco L 2001 *AIAA J.* **39** 2366–2373
[31] Bagheri S, Schlatter P, Schmid P J and Henningson D S 2009 *J. Fluid Mech.* **624** 33–44
[32] Meyer K E, Pedersen J M and Özcan O 2007 *J. Fluid Mech.* **583** 199–227
[33] Alvi F, Ladd J and Bower W 2002 *AIAA J.* **40** 599–609